Applied Surface Science 525 (2020) 146563

Contents lists available at ScienceDirect

Applied Surface Science

journal homepage: www.elsevier.com/locate/apsusc

Constructing volcanic-like mesoporous hard carbon with fast electrochemical kinetics for potassium-ion batteries and hybrid capacitors

Yang Liu[a], Qiang Ru[a,*], Yuqing Gao[a], Qinyou An[b], Fuming Chen[a], Zhenglu Shi[a], Minhui Zheng[a], Zikang Pan[a]

[a] Guangdong Engineering Technology Research Center of Efficient Green Energy and Environmental Protection Materials, Guangdong Provincial Key Laboratory of Quantum Engineering and Quantum Materials, School of Physics and Telecommunication Engineering, South China Normal University, Guangzhou 511400, China
[b] State Key Laboratory of Advanced Technology for Materials Synthesis and Processing, Wuhan University of Technology, Wuhan 430070, China

ARTICLE INFO

Keywords:
Carbon anode
Polyimide
Potassium ion batteries
Potassium ion hybrid capacitors
Boosting potassium-ion storage

ABSTRACT

Potassium-ion batteries are considered as one of safe and low-cost alternatives to the traditional lithium-ion batteries. However, the sluggish potassium ion kinetics, drastic volume variation and inferior cyclic reversibility hinder the further development for the commercial applications. Herein, a new type of polyimide-inspired volcanic rock-like carbon is synthesized by pyrolyzing N/O-rich polymer precursor of polymeric 1, 4, 5, 8-Naphthalenetetracarboxylic dianhydride (PNTCDA). The synergetic effect of the mesoporous construction, the prominent capacitance and the ameliorated conductivity endows PNTCDA@900 with boosted potassium-ion electrochemical properties. As anodes for PIBs, the discharge capacity of 185.3 mAh g^{-1} can be achievable after 100 cycles at a current density of 0.05 A g^{-1}, and the superior reversible capacity of 81 mAh g^{-1} is obtained even after 4000 cycles at a high current density of 2 A g^{-1}. The cell can be operated in a reliable environmental adaptability with 115–205 mAh g^{-1} from −5 °C~70 °C at 0.1 A g^{-1}. Furthermore, when applied to potassium-ion hybrid capacitors with active carbon as cathode, PNTCDA@900 delivers a reversible capacity of 53.5 mAh g^{-1} after 800 cycles at 2 A g^{-1}. The current work will be significant for the development of potassium-ion storage.

1. Introduction

Lithium-ion batteries (LIBs) with high energy and power densities have been commercially popularized in portable electronics and electric vehicles [1–4]. However, the further development of LIBs will be restricted in fields of large-scale energy supply equipment and sustainable utilization because of the high cost, scarcity and limited distribution of lithium source [5]. Right now, much attention is paid to other alkaline metals with abundant reserves in nature and similar electrochemical properties to lithium [6–11]. Recently, potassium-ion batteries (PIBs) as a competitive candidate to LIBs are proposed and present a fast-growing trend towards the prospective applications. Unfortunately, the sluggish potassium ion kinetics and irreversible volume swelling caused by the large K-ion radius (~1.38 Å) usually deteriorate the structural stability and decrease an inferior potassium-ion storage performance. The exploration of a feasible anode with excellent cycling durability and superior rate capability is a hot topic in PIBs [12–17]. Carbonaceous materials have the promising virtues like the low potential, inexpensiveness, high accessibility and eco-friendliness [18–23], compared with other anodes such as metal phosphide, metal sulfide, metallic oxide and alloy compound. However, the traditional graphite materials without modified treatments can hardly accommodate the large-sized K-ion due to the limited interlayer spacing [4,24]. The carbonaceous materials usually are subject to some serious drawbacks like limited cycles and inferior K-ion storage capability.

Recently, some novel carbon-based anodes are reported with the proper modification to obtain an appealing performance in K-ion storage. For instance, Yang et al. presented a hierarchical porous hard carbon anode with N, O-doping in PIBs [25], which can deliver the capacity of 230.6 mAh g^{-1} at 50 mA g^{-1} after 100 cycles and 118 mAh g^{-1} at 3 A g^{-1}. Jian et al. proposed the hard-soft carbon composite as anodes for PIBs, and a capacity of ~200 mAh g^{-1} at 0.2 C was demonstrated after 400 cycles [26]. Ryan et al synthesized a binder-free N, O-rich carbon nanofiber anode by the electrospinning of polyacrylonitrile polymer and subsequent carbonization, which showed the capacity of 160 mAh g^{-1} at 279 mA g^{-1} after 100 cycles [27]. Therefore, the heteroatom doping may be a suitable route for the enhancement of K-ion electrochemical storage.

* Corresponding author at: School of Physics and Telecommunication Engineering, South China Normal University, Guangzhou 511400, China.
E-mail address: rq7702@yeah.net (Q. Ru).

https://doi.org/10.1016/j.apsusc.2020.146563
Received 20 March 2020; Received in revised form 30 April 2020; Accepted 30 April 2020
Available online 05 May 2020
0169-4332/

In this work, we synthesize the polyimide-inspired volcanic rock-like carbon material with N/O doping and investigate the applications for PIBs and potassium-ion hybrid capacitors (PIHCs). The K-ion storage capability and diffusion kinetics are greatly promoted, and the excellent electrochemical performance is obtained. In PIBs, the discharge capacity of 185.3 mAh g^{-1} is exhibited after 100 cycles at 0.05 A g^{-1}. Even under a high current density of 2 A g^{-1}, the reservable specific capacity of 81 mAh g^{-1} is obtained over 4000 cycles. Impressively, the current system can be operated in the wide temperature range from −5 °C~70 °C, and the efficient charge capacities of 115–205 mAh g^{-1} can be maintained at a current density of 0.1 A g^{-1}. Moreover, PIHCs with PNTCDA@900 as anode and active carbon (AC) as cathode are assembled as the novel high-power energy storage device. At various current densities of 0.1, 0.2, 0.5, 1.0 A g^{-1}, PIHCs show the discharge capacities of 128.2 mAh g^{-1}, 118 mAh g^{-1}, 104.5 mAh g^{-1}, 92 mAh g^{-1}. In a long cycling test, PIHCs also exhibit an excellent performance with the reversible capacity of 53.5 mAh g^{-1} at 2 A g^{-1} after 800 cycles. The current study shows a remarkable potential of doped carbon materials for applications in PIBs and PIHCs, which may broaden the prospective road to design more effective carbon-based electrodes.

2. Experimental

2.1. Material synthesis

Ethylenediamine (EDA, AR) and N-methyl pyrrolidone (NMP, 99.5%) are obtained from Aladdin (Shanghai, China). 1, 4, 5, 8-naphthalenetetracarboxylic dianhydride (NTCDA, 97%) is purchased from Energy Chemical (Shanghai, China). The specific surface area of commercial AC (YEC-8, Yihuan Carbon Co., Ltd) is about 2000–2500 m^2 g^{-1}.

2.1.1. Preparation of PNTCDA, NTCDA@900 and PNTCDA@900

The synthesis procedure is shown in Fig. 1. The polymeric precursor PNTCDA was fabricated by the polymerization reaction between NTCDA and EDA in equimolar amounts (10 mmol), under a reflux in solvent of NMP (30 ml) with N_2 at 200 °C for 8 h. Then the collection was washed with NMP and ethanol for several times to remove residual NTCDA, then dried at 120 °C in a vacuum oven overnight. The final product (PNTCDA@900) was synthesized by pyrolyzing PNTCDA at 900 °C for 5 h in N_2 atmosphere. The similar preparation process of NTCDA@900 is used by pyrolyzing NTCDA.

2.2. Material characterizations

X-ray diffraction (XRD, BRUKER, D8 ADVANCE) instrument was carried out to analyze the crystal structure with the scan rate of 2° min^{-1}. The morphology and chemical state were analyzed by field emission scanning electron microscopy equipped with energy dispersive spectrometer (FESEM; ZEISS, ULTRA 55) and X-ray photoelectron spectrometer (XPS; Thermo fisher Scientific, K-Alpha), respectively. Specific surface area and pore diameter distribution of Brunauer-Emmett-Teller (BET) were obtained by JW-BK200C (JWGB Sci.&Tech. Co., Ltd, Beijing). Fourier transform infrared spectroscopy (FTIR) and Raman spectra measurement were conducted by inVia (Renishaw, U.K.) and Nicolet 6700 (Thermo Nicolet, America), respectively.

2.3. Electrochemical measurements

For PIBs, PNTCDA@900, acetylene black and carboxymethyl cellulose were mixed with deionized water to form the slurry in a weight ratio of 8:1:1. After vigorously stirring, the slurry was pasted onto copper foil and transferred to a vacuum oven at 60 °C overnight. Metallic potassium as counter electrode, the mass of the active material for anode is 0.35–0.56 mg cm^{-2}. For the cathode fabrication of PIHCs, AC, acetylene black and polyvinylidene fluoride were mixed in a weight ratio of 8:1:1 with the solvent of N-methyl-2-pyrrolidone. The prepared slurry was coated on aluminum foil and dried at 60 °C in vacuum oven. All tests were obtained by CR2032 coin cells, which were assembled in the argon-filled glove box (MBRAUNLABstar). The separator is glass microfibers filters (Whatman) and the electrolyte is 0.8 M KPF_6 in ethylene carbonate (EC)/diethyl carbonate (DEC) (1:1 by volume).

For PNTCDA@900 anode, the galvanostatic discharge/charge profiles and rate performances were tested by NEWARE battery testing system with the voltage of 0.01–2.0 V. A broader voltage window of 0.01–3.0 V was applied to the long cycle measurement. For PIHCs and AC cathodes, the experimental voltage was set to 0.01–3.5 V and 2.5–4.5 V, respectively. Cyclic voltammetry (CV) measurement and electrochemical impedance spectroscopy (EIS) analysis were employed by Solartron 1470E electrochemical workstation. Before assembling PIHCs, cathode (AC) and anode (PNTCDA@900) were pre-cycled in half-cell for 5 cycles, and mass ratio of cathode and anode was around 6:1. The specific capacities of PIBs and PIHCs were calculated based on the mass of anode materials.

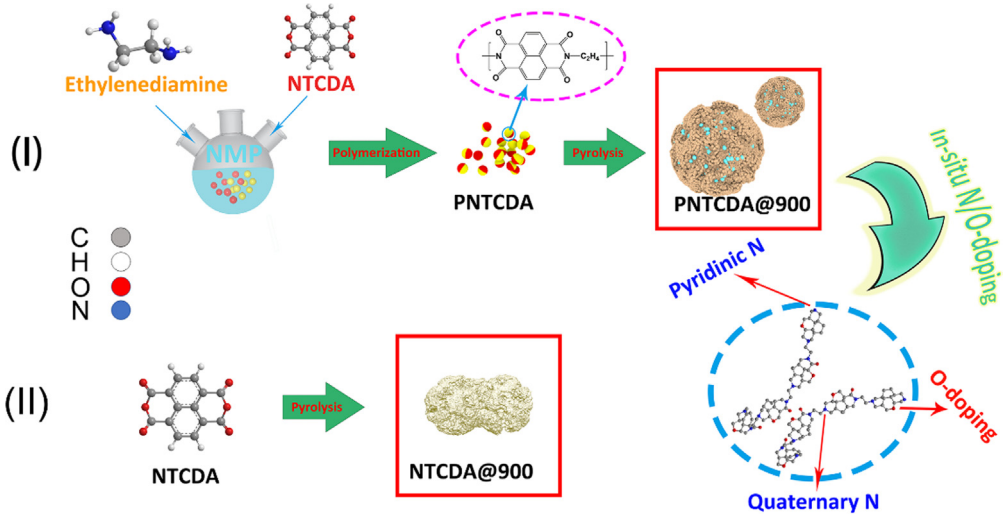

Fig. 1. Schematic illustration of the synthesis process for NTCDA@900, PNTCDA and PNTCDA@900.

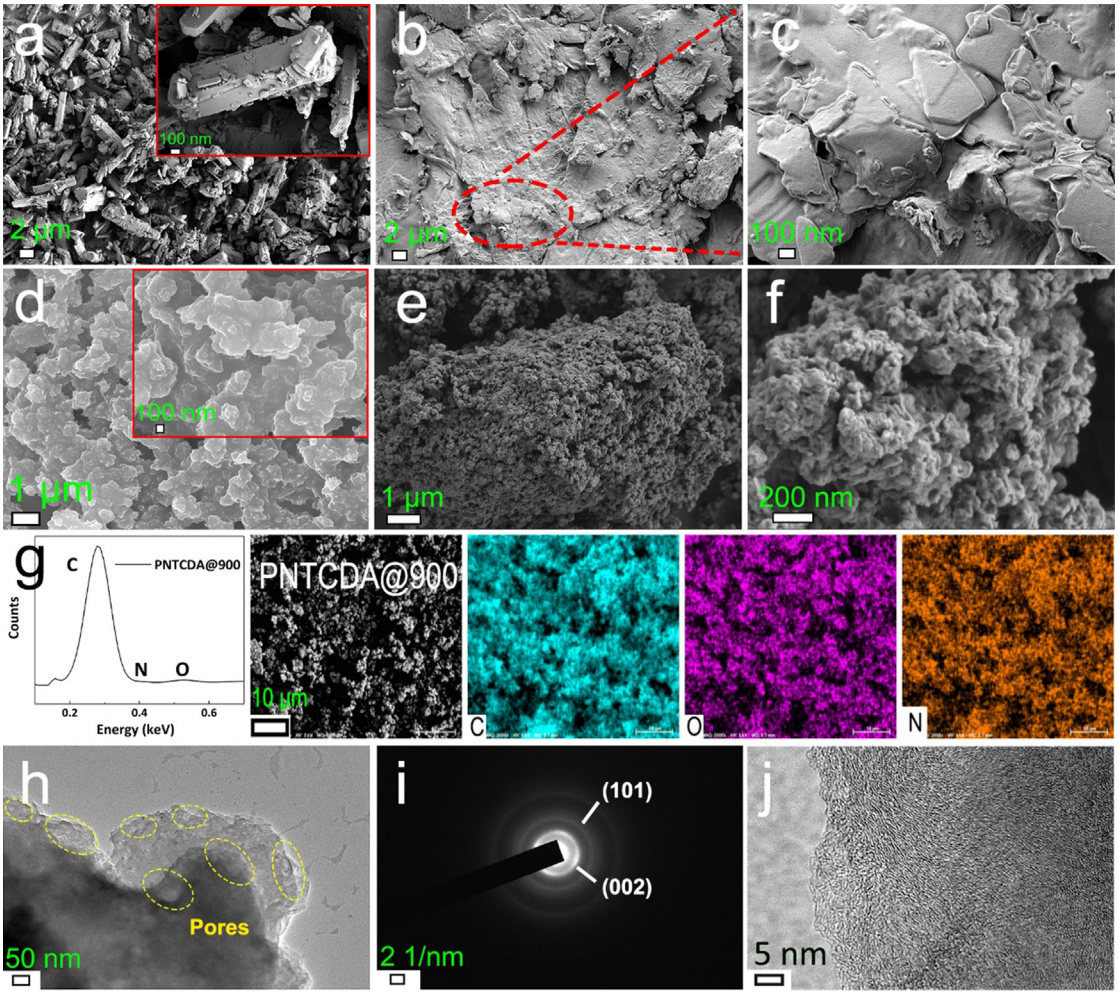

Fig. 2. SEM images of (a) NTCDA, (b-c) NTCDA@900, (d) PNTCDA and (e-f) PNTCDA@900. (g) Energy dispersive spectrum and elemental mapping graphs of PNTCDA@900. (h-j) TEM image, SAED pattern and high-resolution TEM (HRTEM) image of PNTCDA@900.

3. Result and discussion

Fig. 2a presents the disorganized distribution of rod-like NTCDA at the scale of 2 μm. After pyrolyzed at 900 °C, rod-like shape is converted into the stacked flake structure in Fig. 2b-c. The serious agglomeration is a huge obstacle for the transfer and diffusion kinetics of potassium ion [28]. PNTCDA polymerized from NTCDA and EDA displays a squama-like fashion in Fig. 2d. In Figs. S1 and S2 (Supplementary Materials), energy dispersive spectrum of PNTCDA shows the operable in-situ introduction of N/O atoms, and element mapping graphs demonstrate a uniform distribution of C, N and O elements. As shown in Figs. 2e-f and S3 (Supplementary Materials), the pyrolyzed PNTCDA@900 illustrates a volcanic rock-like morphology with rough surface due to the gas release and exfoliation under a high temperature, which can cause the plentiful mesopores for fast ion transport. Furthermore, homogeneous distributions of C, N and O elements are detected in elemental mapping images of PNTCDA@900 in Fig. 2g, which also indicates the availability of N/O doping during the pyrolysis process. As a comparison, the stacked structure of NTCDA@900 can be observed in Fig. S4a-c (Supplementary Materials). On the contrary, abundant mesopores emerge on the surface of PNTCDA@900 in Fig. 2h, which can effectively ameliorate the issue of sluggish potassium kinetics at a high current density. Selected area electron diffraction (SAED) spectra of PNTCDA@900 and NTCDA@900 are shown in Figs. 2i and S5 (Supplementary Materials). The dispersive diffraction rings of (0 0 2) and (1 0 1) planes display a hybrid state of crystallization and amorphization. Furthermore, as shown in Fig. 2j, the narrow-selected HRTEM of PNTCDA@900 shows an irregular carbon array accompanied by a partially ordered interlayer structure, which is consistent with the SAED analysis.

In Fig. 3a-c, PNTCDA@900 with evident type-IV isotherms depicts the larger BET surface area of 33.1 $m^2\ g^{-1}$ and pore volume of 0.082 $cm^3\ g^{-1}$ than NTCDA@900 (5.2 $m^2\ g^{-1}$ and 0.082 $cm^3\ g^{-1}$). The pore size of PNTCDA@900 is 35.56 nm, which firmly supports the presence of mesoporous structure [29]. This BET surface area of 33.1 $m^2\ g^{-1}$ is closer to the other reported value of 54.3 $m^2\ g^{-1}$ of hierarchically porous N-doped carbon fibers [30], which can be expected to own more reaction sites and better electrolyte infiltration to a certain extent. However, it is hard to seek the hysteresis loop in NTCDA@900 sample. The low specific surface area and specific pore volume of NTCDA@900 confirm the compacted flake structure with the absence of pores in SEM and TEM analysis.

As shown in Fig. 3d, XPS survey of PNTCDA@900 indicates the atomic ratios of C, N and O elements are 93.44%, 3.33% and 3.24%, respectively. The C 1s spectrum of PNTCDA@900 in Fig. 3e can be split into three peaks of C-C (284.8 eV), C-N (286.5 eV), and C = O (289 eV). These results strongly confirm the in-situ N/O doping in PNTCDA@900. The high-resolution N 1s spectrum can be deconvoluted into two types of N species in Fig. 3f, which are assigned to 398.2 eV of pyridinic N (N-6; relative peak area of 15.5%) and 401.0 eV of quaternary N (N-Q; relative peak area of 84.5%), respectively. Besides, pyridinic N is usually located in the edges of defective carbon layers. Quaternary N is

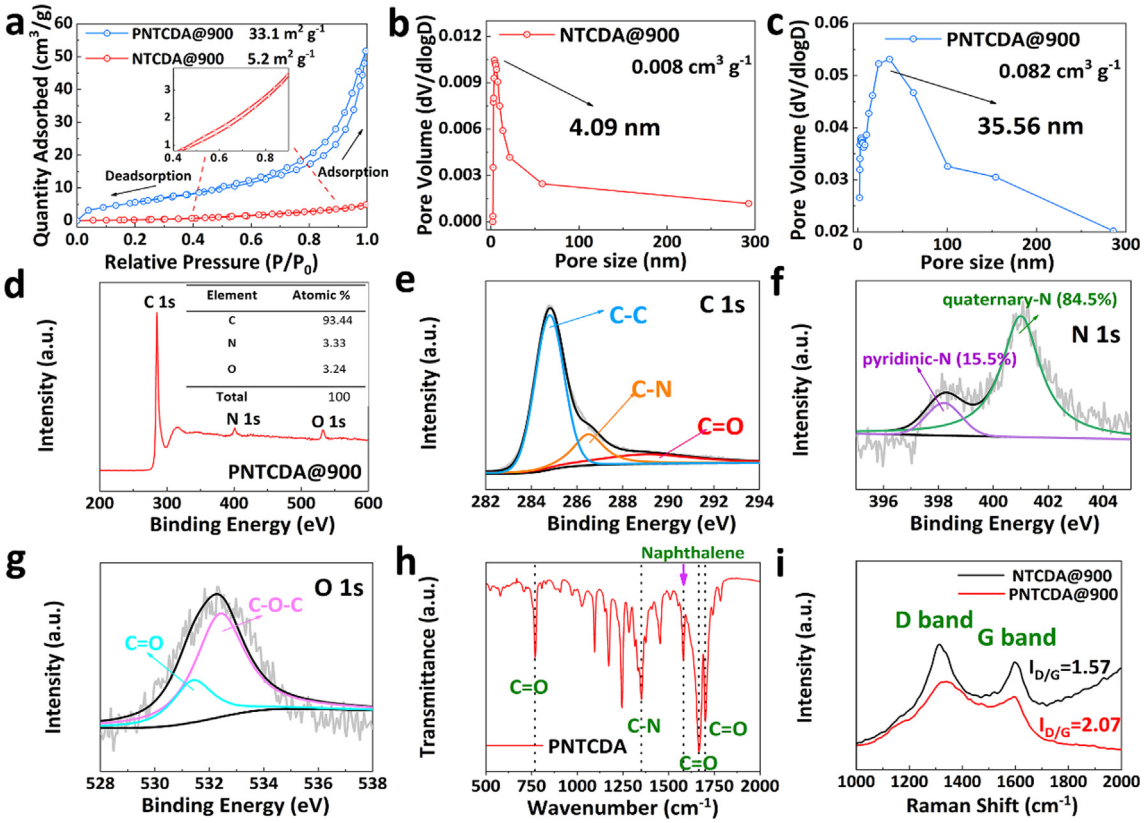

Fig. 3. (a) N_2 adsorption–desorption isotherm of NTCDA@900 and PNTCDA@900. (b-c) Pore size distribution. (d) XPS survey spectrum of PNTCDA@900. The high-resolution XPS spectra of (e) C 1s, (f) N 1s and (g) O 1s. (h) FTIR spectrum of PNTCDA. (i) Raman spectra of NTCDA@900 and PNTCDA@900.

located in the carbon planes and combined with carbon atoms by the sp^2 bonds [32]. The dominant N-Q proportion of 84.5% in PNTCDA@900 is ascribed to the converting of O = C-N-C = O (imide group) to N-Q. In Fig. 3g, O 1s spectrum is split into two peaks of C = O carbonyl group at 531.4 eV and C-O-C ether group at 532.4 eV. According to previous reports [32–34], the introduction of N and O elements in carbon materials can produce abundant defects, form more K^+ active sites, change the original electron donor properties and boost the wettability of carbon. These advantageous changes can accelerate the diffusion of K ions, strengthen the surface-induced capacitance, enhance the electronical conductivity and decrease the inert surface area of carbon, respectively. Hence, the effective N/O-doped modification will make a tremendous contribution to promote the potassium-ion storage performance of PNTCDA@900.

FTIR spectrum is shown in Fig. S6 (Supplementary Materials) and Fig. 3h. O = C-O-C = O bond of NTCDA at 1039 cm^{-1} will be transformed to the imide group of O = C-N-C = O after a polymerization process, and the resultant C-N bond observed at 1353.8 cm^{-1} shows the successful synthesis of PNTCDA [28,32,35]. Raman spectra in Fig. 3i are used to clarify the graphitization characteristics and disordered aromatic structure [36–38]. The higher D/G peak intensity ratio of PNTCDA@900 ($I_{D/G}$ = 2.07) represents a lower graphitization degree than NTCDA@900 ($I_{D/G}$ = 1.57), which results from the introduction of N and O heteroatom. Whereas, N atoms embedded in carbon lattice can not only optimize the electronic conductivity, but also bring in more edges/defects for K^+ adsorption to promote capacitance behaviors [32,39].

3.1. Potassium-ion batteries performance

In Fig. 4a, the original NTCDA shows three main diffraction peaks at 12.2°, 23.6° and 24.6°, corresponding to lattice planes of (1 0 0), (1̄ 1 2) and (2 0 0), respectively [40]. NTCDA@900 and PNTCDA@900 possess the similar XRD patterns with two broad peaks around 26° and 44°, indicating a hybrid structure of crystallization and amorphization.

After 50 cycles, ex-situ XRD patterns of PNTCDA@900 are displayed in Fig. S7 (Supplementary Materials), which are used to investigate the mechanism of K insertion/extraction inside carbon matrix. In contrast to pristine state, both potassiation and depotassiation processes show the SEI layer peaks at 19.8°, 22.9°, and 32.6°, which is mainly caused by the complex side reaction between electrode and electrolyte. After fully discharging to 0.01 V, two diffraction peaks located at 16.9° and 33.3° are well consistent with the KC_8 phase [32]. Then KC_8 characteristic peaks disappear after fully charging to 2.0 V, and the complete depotassiation curve keeps a similar shape with pristine state, which indicates the good cyclic reversibility of PNTCDA@900.

Figs. 4b and S8a (Supplementary Materials) demonstrate typical CV curves of PNTCDA@900 and NTCDA@900 between 0.01 V and 2 V at the scan rate of 1 mV s^{-1}. During the first cathodic scan of PNTCDA@900, the irreversible capacity loss appears around 0.5 V, which contains the complex formation of SEI film and excessive K-insertion [31]. Accordingly, the anodic peak at the first cycle is located at 0.75 V and then shifts to 0.55 V in the following cycles, due to the repeatable K-extraction process. PNTCDA@900 keeps the similar CV curves in the succeeding cycles, presenting a good cyclic durability. There are no obvious redox peaks of NTCDA@900 in CV curves because of the weak K-de/intercalation reaction. Figs. S8b and S9 (Supplementary Materials) display typical galvanostatic charge–discharge profiles of NTCDA@900 and PNTCDA@900 under a current density of 0.05 A g^{-1}. The capacity loss of electrodes in first cycle is considered to be the formation of solid electrolyte interphase (SEI) and irreversible K-insertion among the carbon layers. Compared to the second cycle, capacity retention ratios of PNTCDA@900 are 67% (25th), 71.8% (50th), and 68% (100th), higher than those of NTCDA@900 (64%, 45.7%, and 43.8%). And the anode shows a high durability and large capacity for long cycling. In addition, these charge/discharge profiles exhibit a

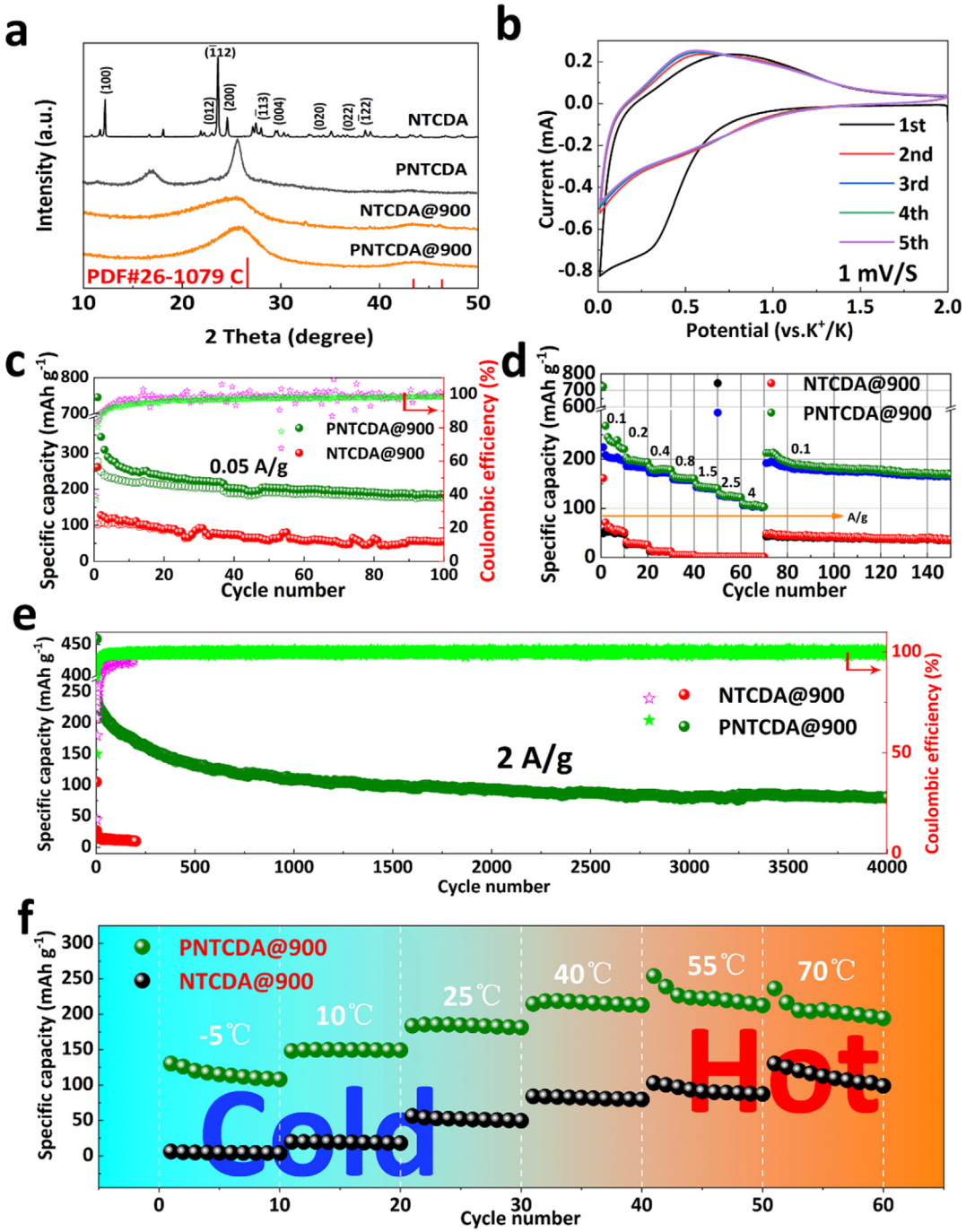

Fig. 4. (a) XRD patterns of NTCDA, PNTCDA, NTCDA@900 and PNTCDA@900. (b) CV curves of PNTCDA@900 at 1.0 mV s^{-1}. The electrochemical performance of NTCDA@900 and PNTCDA@900 electrodes in PIBs: (c) Cycle performance at 0.05 A g^{-1}. (d) Rate performance from 0.1 to 4 A g^{-1}. (e) Long cycle property at 2 A g^{-1}. (f) Cycling at different temperatures from −5 °C to 70 °C.

characteristic slope since the second cycle, which is similar to previous reports of non-graphitic carbon materials [41,42].

The cyclic contrasts of NTCDA@900 and PNTCDA@900 are shown in Fig. 4c. PNTCDA@900 supplies a discharge capacity of 185.3 mAh g^{-1} after 100 cycles at 0.05 A g^{-1} with a high coulombic efficiency (CE) of 98.15%. As for rate performance shown in Fig. 4d, PNTCDA@900 indicates outstanding specific capacities of 220.7 mAh g^{-1}, 193.9 mAh g^{-1}, 178.3 mAh g^{-1}, 160.6 mAh g^{-1}, 140.5 mAh g^{-1} and 122.6 mAh g^{-1} at the current densities of 0.1, 0.2, 0.4, 0.8, 1.5 and 2.5 A g^{-1}, respectively. Even at the high current density of 4 A g^{-1}, a maintainable capacity of 103 mAh g^{-1} is obtained while NTCDA@900 can hardly provide any capacity. When the current density comes back to 0.1 A g^{-1}, PNTCDA@900 keeps the stable capacity of 169 mAh g^{-1} after 150 cycles. The prominent achievements of PNTCDA@900 can profit from the heteroatom doping and pore-forming preparation. The N/O doping is beneficial to enhance the conductivity of electrodes and introduce more defects. Mesoporous structure can shorten the transmission path of K ions to improve rate performance, and enlarge contact area for the electrolyte to obtain a better electrochemical property. On the other hand, the compacted microstructure without heteroatom doping is considered as the key cause for NTCDA@900 to block the ion transport and result in poor performance. Hence, the N/O doping design and mesoporous structure play a primary role in increasing energy storage sites and electrical/ionic conductivities, presenting the effective

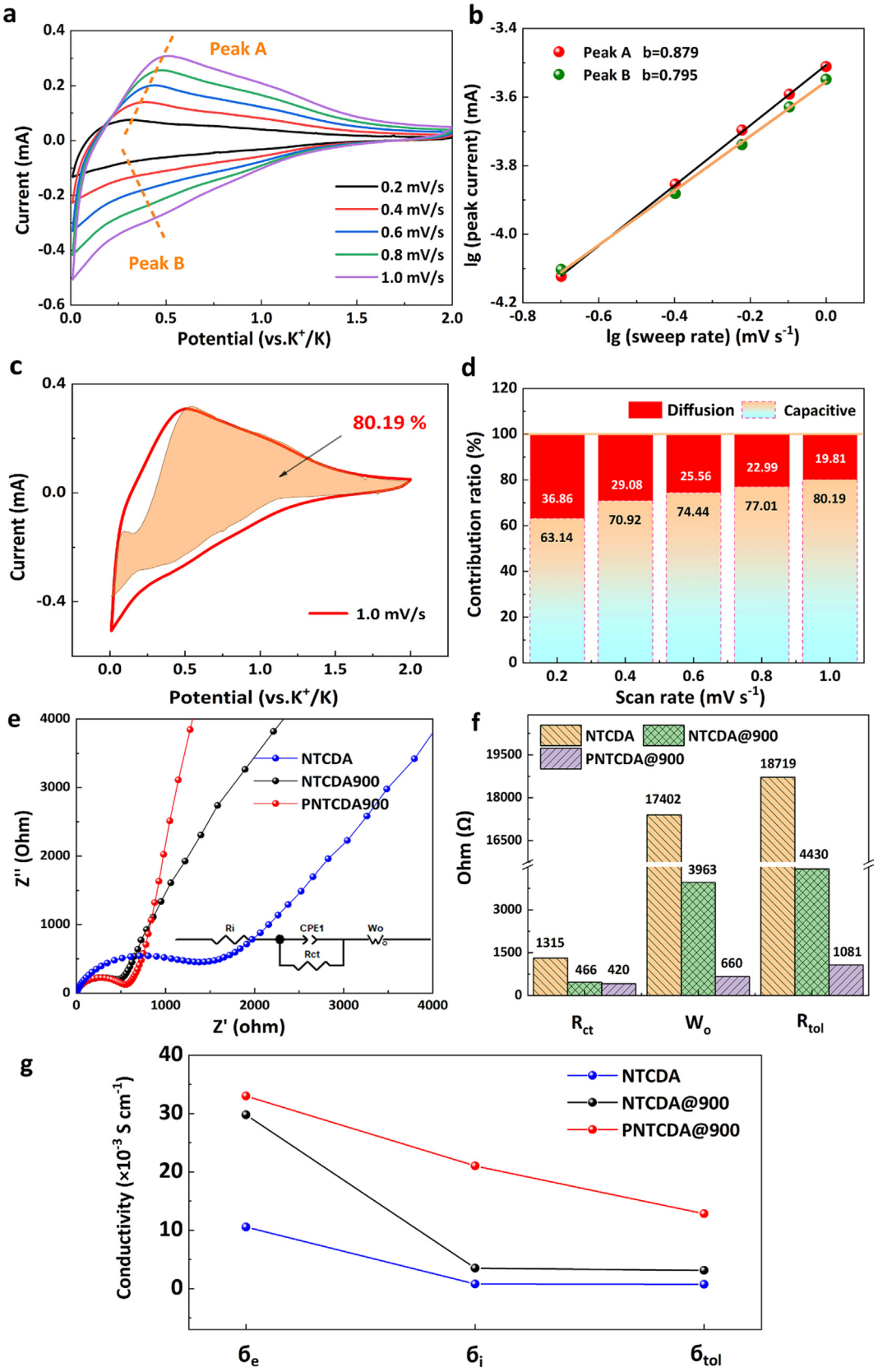

Fig. 5. Electrochemical kinetic analysis of PNTCDA@900 in surface-dominated potassium ion storage: (a) CV curves at a scan rate from 0.2 to 1.0 mV s^{-1}. (b) The fitted b-value plots for anodic and cathodic scan. (c) CV curve and the proportion of capacitive fraction at a scan rate of 1.0 mV s^{-1}. (d) Contribution ratios of the capacitive and diffusion-controlled charge storage at various scan rates. EIS analysis of NTCDA, NTCDA@900 and PNTCDA@900 in potassium ion storage: (e) Nyquist plots and the equivalent circuit. (f) Different circuit parameters values of three materials. (g) The calculated result of electron, ion and total conductivities.

improvements for the higher practical capacity and quicker potassium kinetics. That is also reflected in the results of long cycling performance.

The long-term cycles are performed under a high current density of 2 A g^{-1} and at a broader voltage of 0.01–3.0 V as shown in Fig. 4e. After 4000 cycles, PNTCDA@900 shows an outstanding reversible capacity of 81 mAh g^{-1} with a CE of 99.3%, but NTCDA@900 only shows the very low capacity of 1.6 mAh g^{-1} after 200 cycles. Subsequently, the high-low temperature performance is measured at a temperature range from −5 °C to 70 °C in Fig. 4f. PNTCDA@900 keeps the high charge capacities of 115 mAh g^{-1}, 149.5 mAh g^{-1}, 184.5 mAh g^{-1}, 216.4 mAh g^{-1}, 222.2 mAh g^{-1} and 205.8 mAh g^{-1} at different temperatures of −5 °C, 10 °C, 25 °C, 40 °C, 55 °C and 70 °C, respectively. Hence, PNTCDA@900 delivers an undiminished K-storage capability in a wide working temperature range.

To explore the in-depth mechanism of PNTCDA@900 in potassium ion storage, CV analysis has been carried out in Fig. 5a with the incremental sweep rates from 0.2 to 1.0 mV s^{-1}. The capacitive contribution can be calculated based on following equation:

$$i = av^b \tag{1}$$

where i represents peak current, a and b represent adjustable constants, and v represents scan rate. Moreover, the slope closing to 1.0 means a surface capacitance-controlled response, otherwise approaching to 0.5 indicates a diffusion-controlled reaction. The plots applied to the peak current of PNTCDA@900 are shown in Fig. 5b. The b-values of two fitted plots are 0.879 and 0.795, corresponding to anodic and cathodic peaks, respectively. The dominated capacitive behaviors have a significant contribution to promote the potassium storage of PNTCDA@900. Furthermore, the contribution ratio of capacitive behavior to overall capacity can be calculated by the equation as follows:

$$i = k_1 v + k_2 v^{\frac{1}{2}} \tag{2}$$

where i represents the current response, v represents scan rate, $k_1 v$ represents capacitive reactions, and $k_2 v^{1/2}$ stands for the part of diffusion-controlled behavior. As shown in Fig. 5c, the capacitive contribution (orange region) of PNTCDA@900 for total capacity is 80.19% at the scan rate of 1 mV s^{-1} (other scan rates shown in Fig. S10, Supplementary Materials). The relative ratios of capacitance and diffusion contribution at overall scan rates are obtained in Fig. 5d. Obviously, the ratios of capacitance contribution rise from 63.14% to 80.19%, representing the gradual increase in capacitive effect.

EIS measurement has been performed to study the ion/electron dynamics. Nyquist plots of three electrodes are shown in Fig. 5e with a well-fitted equivalent circuit, and all circuit parameters values are recorded in Table 1, including the solution resistance (R_s), charge transfer resistance (R_{ct}), diffusion impedance (W_o) and total resistance ($R_{tol} = R_s + R_{ct} + W_o$). Three significant circuit resistances are displayed in Fig. 5f. To evaluate the electrochemical kinetics, equivalent conductivities are obtained via the equation as below:

$$\sigma = l/(R\hat{A}\cdot S) \tag{3}$$

where σ equals to σ_e (electronic conductivity), σ_i (ionic conductivity) and σ_t (total conductivity), respectively. l represents the thickness of electrode. R represents impedance and S represents the cross-sectional area of the electrode material. The calculated results of conductivities are also shown in Table 1 and plotted in Fig. 5g.

As shown in Fig. 5g, compared with original NTCDA, NTCDA@900 and PNTCDA@900 show the enhanced electrical conductivity. But the dissimilarity of structure in two pyrolysis products leads to a quite different σ_i. It should be explained that the compacted microstructure of NTCDA@900 will hamper the ion transport and lead to a poor rate property. On the contrary, in-situ N/O doped construction and mesoporous morphology of PNTCDA@900 occupy the predominant contributions to accelerate K-ion diffusion, demonstrating the much higher ion conductivity than NTCDA@900. Thus, PNTCDA@900 delivers the optimal electronic and ionic diffusion dynamics.

3.2. Potassium-ion hybrid capacitors performance

Given the discussion above, PNTCDA@900 anode with strong surface capacitance and detectable K-ion de/intercalation shows the combination of capacitance and battery-type energy storage. On the other hand, AC is considered as a proper cathode, which possesses the superb adsorption/desorption reaction of PF_6^- due to its vast surface area [43]. Therefore, PIHCs are assembled by employing PNTCDA@900 as anode and AC as the cathode. To achieve a good capacity-matched balance between cathode and anode, AC and PNTCDA@900 half-cell are conducted at a same current density of 0.1 A g^{-1}. As shown in Fig. 6a and S11 (Supplementary Materials), AC and PNTCDA@900 exhibit the stable capacity of 38 mAh g^{-1} and 200 mAh g^{-1} after 50 cycles at 0.1 A g^{-1}, respectively. For AC cathode, both the linear slope in Fig. 6b and rectangle-like shape in Fig. 6c demonstrate an ideal capacitive behavior. For the PIHCs (Fig. 6d), it displays the discharge capacities of 128.2 mAh g^{-1}, 118 mAh g^{-1}, 104.5 mAh g^{-1}, 92 mAh g^{-1}, 104.1 mAh g^{-1}, 117.7 mAh g^{-1}, 127.8 mAh g^{-1} at various current densities of 0.1, 0.2, 0.5, 1.0, 0.5, 0.2, 0.1 A g^{-1}, revealing an excellent rate recyclability. Based on U-t plot at different current densities (Fig. 6e), the energy density (E, Wh kg^{-1}) and power density (P, W kg^{-1}) can be calculated by these equations below and shown in Table 2:

$$E = \int_{t1}^{t2} IVdt = \Delta V \times \frac{I}{m} \times t \tag{4}$$

$$P = \frac{E}{t} \tag{5}$$

where I is the charge/discharge current, V is the discharge voltage, m is the total mass containing cathode and anode, and t corresponds to the discharge time. PIHCs deliver the promising energy density of 36.4 Wh kg^{-1} at a power density of 161.8 W kg^{-1}. It also has 20.2 Wh kg^{-1} even though at a higher power density of 600.0 W kg^{-1}. With respect to CV curves of PIHCs (Fig. 6f), the rectangle-like shape at scan rates from 0.2 to 20 mV s^{-1} proves that it is operated by the non-faradic reaction. In Fig. 6g, galvanostatic charge–discharge profiles of PIHCs show the overlapped and typical linear slope, at the same time, the cyclic capacity keeps an undiminished trend after 50 cycles. The energy storage mechanism of PIHCs can be described as Fig. 6h. PNTCDA@900 anode exhibits a batteries-type reaction with de/intercalation and adsorption/desorption of K ions. Meanwhile, AC cathode shows a pure capacitive behavior of adsorption/desorption of PF_6^-. During the long-term cycling in Fig. 6i, PIHCs deliver the first charge/discharge capacity of 107.7 mAh g^{-1} / 75.1 mAh g^{-1} with a good CE of 69.7%. After 800 cycles, it still maintains a predominant reversible capacity of 53.5 mAh g^{-1} at 2 A g^{-1} with a CE of 98%. These properties have exhibited a

Table 1
All parameters values and conductivities of equivalent circuit for three materials.

Sample	R_s (Ω)	R_{ct} (Ω)	$б_e$ ($\times 10^{-3}$ S·cm^{-1})	W_o (Ω)	$б_i$ ($\times 10^{-3}$ S·cm^{-1})	R_{tol} (Ω)	$б_t$ ($\times 10^{-3}$ S·cm^{-1})
NTCDA	2.087	1315	10.56	17,402	0.80	18719.08	0.74
NTCDA@900	1.325	466.1	29.80	3963	3.50	4430.42	3.13
PNTCDA@900	0.729	420.6	33.02	660.2	21.04	1081.52	12.84

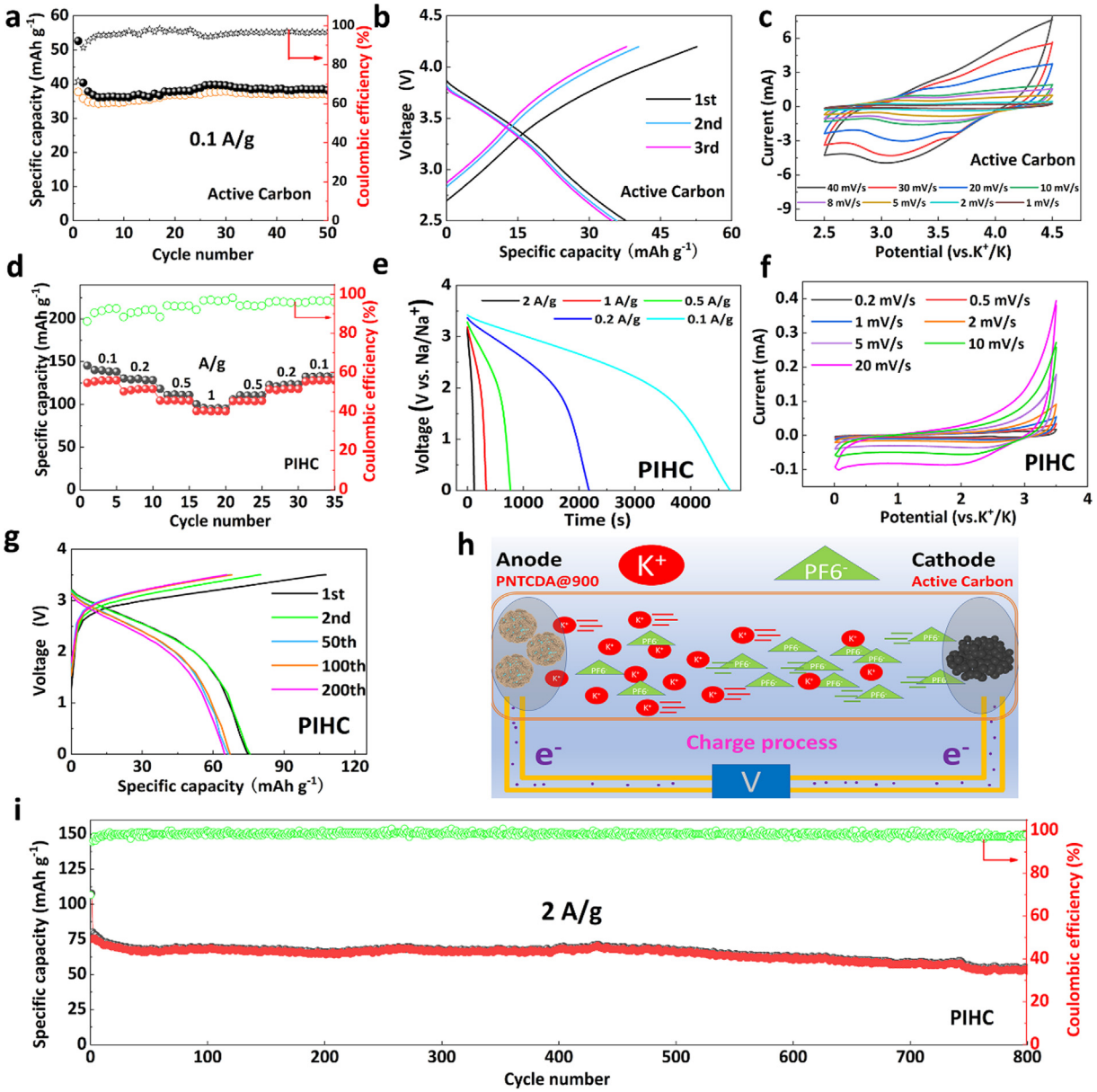

Fig. 6. Half-cell performances of active carbon: (a) Cycling at 0.1 A g^{-1}. (b) Galvanostatic charge–discharge profiles. (c) CV curves with voltage of 2.5–4.5 V at scan rates from 1.0 to 20 mV s^{-1}. Performances of PIHCs comprising PNTCDA@900 anode and active carbon cathode: (d-e) Rate property at 0.1 to 1 A g^{-1} and corresponding galvanostatic charge–discharge profiles. (f) CV curves with voltage of 0.01–3.5 V at scan rates from 0.2 to 20 mV s^{-1}. (g) Galvanostatic charge–discharge profiles of 1st, 2nd, 50th, 100th, 200th cycle at 2 A g^{-1}. (h) Schematic illustration of PNTCDA@900//AC PIHCs. (i) Long-term cycling property at 2 A g^{-1}.

Table 2
PIHCs electrochemical performance.

Anode//Cathode	Potential range (V)	E(Wh/kg)	P(W/kg)	Current density(A g^{-1})
PNTCDA@900//AC	0.01–3.5	20.14	600.0	2
		29.3	314.9	1
		34.6	161.8	0.5
		39.8	65.8	0.2
		42.9	32.8	0.1

potential application prospect of PNTCDA@900 materials.

4. Conclusion

Volcanic rock-like PNTCDA@900 carbon anode material was synthesized successfully. Due to the N/O doping, increased conductivity, abundant active sites and strong capacitance effect, the novel anode material can provide an excellent potassium-ion storage performance. As anodes for PIBs, PNTCDA@900 demonstrates a decent capacity of 185.3 mAh g^{-1} after 100 cycles at 0.05 A g^{-1} and rate capacity of 103 mAh g^{-1} at 4 A g^{-1}. During the long-periodic satiability test, it also demonstrates a superior specific capacity of 81 mAh g^{-1} after 4000 cycles at 2 A g^{-1}. In a high-low temperature test, it can keep a stable cycle performance of 115–205 mAh g^{-1} from −5 °C~ 70 °C at 0.1 A g^{-1}. For PIHCs, PNTCDA@900 shows a promising application with the stable cyclicity (53.5 mAh g^{-1} at 2 A g^{-1} after 800 cycles) and applicable energy/power density (36.4 Wh kg^{-1}/161.8 W kg^{-1}). This work may be significant to the development of K-ion storage.

CRediT authorship contribution statement

Yang Liu: Methodology, Data curation, Investigation, Writing - original draft. **Qiang Ru:** Supervision, Funding acquisition, Resources,

Writing - review & editing. **Yuqing Gao:** Investigation, Conceptualization. **Qinyou An:** Supervision, Writing - review & editing. **Fuming Chen:** Conceptualization, Supervision. **Zhenglu Shi:** Software. **Minhui Zheng:** Investigation, Visualization. **Zikang Pan:** Investigation.

Declaration of Competing Interest

The authors declare that they have no known competing financial interests or personal relationships that could have appeared to influence the work reported in this paper.

Acknowledgement

This work was supported by the Natural Science Foundation of Guangdong province [2019A1515011615]; the Scientific and Technological Plan of Guangdong Province [2017A040405047]; the Scientific and Technological Plan of Guangzhou City [201804010169, 201607010274]; and the Department of Education of Guangdong Province [2018KTSCX047].

Appendix A. Supplementary material

Supplementary data to this article can be found online at https://doi.org/10.1016/j.apsusc.2020.146563.

References

[1] H. Yuan, W. Zhang, J.-G. Wang, G. Zhou, Z. Zhuang, J. Luo, H. Huang, Y. Gan, C. Liang, Y. Xia, J. Zhang, X. Tao, Facilitation of sulfur evolution reaction by pyridinic nitrogen doped carbon nanoflakes for highly-stable lithium-sulfur batteries, Energy Storage Mater. 10 (2018) 1–9.
[2] X. Shen, W. Mao, Y. Ma, D. Xu, P. Wu, O. Terasaki, L. Han, S. Che, A hierarchical MFI zeolite with a two-dimensional square mesostructure, Angew. Chem. Int. Ed. Engl. 57 (2018) 724–728.
[3] L. Wu, J. Zheng, L. Wang, X. Xiong, Y. Shao, G. Wang, J.H. Wang, S. Zhong, M. Wu, PPy-encapsulated SnS2 nanosheets stabilized by defects on a TiO_2 support as a durable anode material for lithium-ion batteries, Angew. Chem. Int. Ed. Engl. 58 (2019) 811–815.
[4] M. Li, J. Lu, Z. Chen, K. Amine, 30 Years of lithium-ion batteries, Adv. Mater. 30 (2018) 1800561.
[5] J. Li, L. Shi, J. Gao, G. Zhang, General One-pot synthesis of transition-metal phosphide/nitrogen-doped carbon hybrid nanosheets as ultrastable anodes for sodium-ion batteries, Chemistry 24 (2018) 1253–1258.
[6] Q. Xia, W. Li, Z. Miao, S. Chou, H. Liu, Phosphorus and phosphide nanomaterials for sodium-ion batteries, Nano Res. 10 (2017) 4055–4081.
[7] C. Wu, S.-X. Dou, Y. Yu, The state and challenges of anode materials based on conversion reactions for sodium storage, Small 14 (2018) 1703671.
[8] Z. Wang, L. Qie, L. Yuan, W. Zhang, X. Hu, Y. Huang, Functionalized N-doped interconnected carbon nanofibers as an anode material for sodium-ion storage with excellent performance, Carbon 55 (2013) 328–334.
[9] K. Share, A.P. Cohn, R. Carter, B. Rogers, C.L. Pint, Role of nitrogen-doped graphene for improved high-capacity potassium ion battery anodes, ACS Nano 10 (2016) 9738–9744.
[10] J. Liu, T. Yin, B. Tian, B. Zhang, C. Qian, Z. Wang, L. Zhang, P. Liang, Z. Chen, J. Yan, X. Fan, J. Lin, X. Chen, Y. Huang, K.P. Loh, Z.X. Shen, Unraveling the potassium storage mechanism in graphite foam, Adv. Energy Mater. 9 (2019) 1900579.
[11] S. Chen, L. Zhao, J. Ma, Y. Wang, L. Dai, J. Zhang, Edge-doping modulation of N, P-codoped porous carbon spheres for high-performance rechargeable Zn-air batteries, Nano Energy 60 (2019) 536–544.
[12] J. Li, W. Qin, J. Xie, H. Lei, Y. Zhu, W. Huang, X. Xu, Z. Zhao, W. Mai, Sulphur-doped reduced graphene oxide sponges as high-performance free-standing anodes for K-ion storage, Nano Energy 53 (2018) 415–424.
[13] J. Hou, C. Cao, F. Idrees, X. Ma, Hierarchical porous nitrogen-doped carbon nanosheets derived from silk for ultrahigh-capacity battery anodes and supercapacitors, ACS Nano 9 (2015) 2556–2564.
[14] Y. Lu, P. Zhou, K. Lei, Q. Zhao, Z. Tao, J. Chen, Selenium phosphide (Se_4P_4) as a new and promising anode material for sodium-ion batteries, Adv. Energy Mater. 7 (2017) 1601973.
[15] B. Cao, Q. Zhang, H. Liu, B. Xu, S. Zhang, T. Zhou, J. Mao, W.K. Pang, Z. Guo, A. Li, J. Zhou, X. Chen, H. Song, Graphitic carbon nanocage as a stable and high power anode for potassium-ion batteries, Adv. Energy Mater. 8 (2018) 1801149.
[16] I. Sultana, M.M. Rahman, Y. Chen, A.M. Glushenkov, Potassium-ion battery anode materials operating through the alloying-dealloying reaction mechanism, Adv. Funct. Mater. 28 (2018) 1703857.
[17] C. Yang, J. Feng, F. Lv, J. Zhou, C. Lin, K. Wang, Y. Zhang, Y. Yang, W. Wang, J. Li, S. Guo, Metallic graphene-like VSe_2 ultrathin nanosheets: superior potassium-ion storage and their working mechanism, Adv. Mater. 30 (2018) 1800036.
[18] Q. Zhao, Y. Meng, J. Li, D. Xiao, Sulfur and nitrogen dual-doped porous carbon nanosheet anode for sodium ion storage with a self-template and self-porogen method, Appl. Surf. Sci. 481 (2019) 473–483.
[19] Y. Lu, D. Li, C. Lyu, H. Liu, B. Liu, S. Lyu, T. Rosenau, D. Yang, High nitrogen doped carbon nanofiber aerogels for sodium ion batteries: synergy of vacancy defects to boost sodium ion storage, Appl. Surf. Sci. 496 (2019) 143717.
[20] J. Serafin, M. Baca, M. Biegun, E. Mijowska, R.J. Kaleńczuk, J. Sreńscek-Nazzal, B. Michalkiewicz, Direct conversion of biomass to nanoporous activated biocarbons for high CO_2 adsorption and supercapacitor applications, Appl. Surf. Sci. 497 (2019) 143722.
[21] C. Li, X. Zhang, K. Wang, X. Sun, Y. Ma, High-power and long-life lithium-ion capacitors constructed from N-doped hierarchical carbon nanolayer cathode and mesoporous graphene anode, Carbon 140 (2018) 237–248.
[22] C. Li, X. Zhang, K. Wang, X. Sun, Y. Ma, High-power lithium-ion hybrid supercapacitor enabled by holey carbon nanolayers with targeted porosity, J. Power Sources 400 (2018) 468–477.
[23] C. Li, X. Zhang, K. Wang, X. Sun, G. Liu, J. Li, H. Tian, J. Li, Y. Ma, Scalable self-propagating high-temperature synthesis of graphene for supercapacitors with superior power density and cyclic stability, Adv. Mater. 29 (2017) 1604690.
[24] A. Eftekhari, Z. Jian, X. Ji, Potassium secondary batteries, ACS Appl. Mater. Interfaces 9 (2017) 4404–4419.
[25] J. Yang, Z. Ju, Y. Jiang, Z. Xing, B. Xi, J. Feng, S. Xiong, Enhanced capacity and rate capability of nitrogen/oxygen dual-doped hard carbon in capacitive potassium-ion storage, Adv. Mater. 30 (2018) 1700104.
[26] Z. Jian, S. Hwang, Z. Li, A.S. Hernandez, X. Wang, Z. Xing, D. Su, X. Ji, Hard-soft composite carbon as a long-cycling and high-rate anode for potassium-ion batteries, Adv. Funct. Mater. 27 (2017) 1700324.
[27] R.A. Adams, J.-M. Syu, Y. Zhao, C.-T. Lo, A. Varma, V.G. Pol, Binder-free N- and O-rich carbon nanofiber anodes for long cycle life K-Ion batteries, ACS Appl. Mater. Interfaces 9 (2017) 17872–17881.
[28] Z. Jian, W. Luo, X. Ji, Carbon electrodes for k-ion batteries, J. Am. Chem. Soc. 137 (2015) 11566–11569.
[29] W. Yang, L. Hou, X. Xu, Z. Li, X. Ma, F. Yang, Y. Li, Carbon nitride template-directed fabrication of nitrogen-rich porous graphene-like carbon for high performance supercapacitors, Carbon 130 (2018) 325–332.
[30] M. Zhang, M. Shoaib, H. Fei, T. Wang, J. Zhong, L. Fan, L. Wang, H. Luo, S. Tan, Y. Wang, J. Zhu, J.W. Hu, B.G. Lu, Hierarchically porous N-doped carbon fibers as a free-standing anode for high-capacity potassium-based dual-ion battery, Adv. Energy Mater. 9 (2019) 1901663.
[31] M. Chen, W. Wang, X. Liang, S. Gong, J. Liu, Q. Wang, S.J. Guo, H. Yang, Sulfur/oxygen codoped porous hard carbon microspheres for high-performance potassium-ion batteries, Adv. Energy Mater. 8 (2018) 1800171.
[32] L. Tao, Y. Yang, H. Wang, Y. Zheng, H. Hao, W. Song, J. Shi, M. Huang, D. Mitlin, Sulfur-nitrogen rich carbon as stable high capacity potassium ion battery anode: Performance and storage mechanisms, Energy Storage Mater. 27 (2020) 212–225.
[33] J. Ruan, Y. Zhao, S. Luo, T. Yuan, J. Yang, D. Sun, S. Zheng, Fast and stable potassium-ion storage achieved by in situ molecular self-assembling N/O dual-doped carbon network, Energy Storage Mater. 23 (2019) 46–54.
[34] G. Lu, H. Wang, Y. Zheng, H. Zhang, Y. Yang, J. Shi, M. Huang, W. Liu, Metal-organic framework derived N-doped CNT@ porous carbon for high-performance sodium-and potassium-ion storage, Electrochim. Acta 319 (2019) 541–551.
[35] L. Fan, R. Ma, J. Wang, H. Yang, B. Lu, An ultrafast and highly stable potassium-organic battery, Adv. Mater. 30 (2018) 1805486.
[36] C. Ma, W. Zhang, Y.S. He, Q. Gong, H. Che, Z.F. Ma, Carbon coated SnO_2 nanoparticles anchored on CNT as a superior anode material for lithium-ion batteries, Nanoscale 8 (2016) 4121–4126.
[37] C. Wang, M. Lan, Y. Zhang, H. Bian, M.-F. Yuen, K. Ostrikov, J. Jiang, W. Zhang, Y.Y. Li, J. Lu, $Fe_{1-x}S$/C nanocomposites from sugarcane waste-derived microporous carbon for high-performance lithium ion batteries, Green Chem. 18 (2016) 3029–3039.
[38] Q. Liu, Y. Wang, L. Dai, J. Yao, Scalable fabrication of nanoporous carbon fiber films as bifunctional catalytic electrodes for flexible Zn-air batteries, Adv. Mater. 28 (2016) 3000–3006.
[39] H. Gu, L. Yang, Y. Zhang, C. Wang, X. Zhang, Z. Xie, J. Wei, Z. Zhou, Highly reversible alloying/dealloying behavior of SnSb nanoparticles incorporated into N-rich porous carbon nanowires for ultra-stable Na storage, Energy Storage Mater. 21 (2019) 203–209.
[40] H. Abdel-Khalek, E. Shalaan, M. Abd-El Salam, A.M. El-Sagheer, A.M. El-Mahalawy, Effect of thermal annealing on structural, linear and nonlinear optical properties of 1, 4, 5, 8-naphthalene tetracarboxylic dianhydride thin films, J. Mol. Struct. 1178 (2019) 408–419.
[41] Y. Xu, C. Zhang, M. Zhou, Q. Fu, C. Zhao, M. Wu, Y. Lei, Highly nitrogen doped carbon nanofibers with superior rate capability and cyclability for potassium ion batteries, Nat. Commun. 9 (2018) 1720.
[42] W. Wang, J. Zhou, Z. Wang, L. Zhao, P. Li, Y. Yang, C. Yang, H. Huang, S. Guo, Short-range order in mesoporous carbon boosts potassium-ion battery performance, Adv. Energy Mater. 8 (2018) 1701648.
[43] D. Qiu, J. Guan, M. Li, C. Kang, J. Wei, Y. Li, Z. Xie, F. Wang, R. Yang, Kinetics enhanced nitrogen-doped hierarchical porous hollow carbon spheres boosting advanced potassium-ion hybrid capacitors, Adv. Funct. Mater. 29 (2019) 1903496.